Scanning Electron Microscopy

Wei Han, Huisheng Jiao and Daniel Fox

1 Introduction

The scanning electron microscope (SEM) is the most widely used tool for characterizing and analyzing the surface of solid samples. It is utilized in many research areas as well as in various industry sectors. Using the SEM, material scientists can study nanoscale features of their samples, which enables them to gain knowledge of the formation and properties of the sample. The SEM is also an indispensable tool to investigate biological samples and it facilitates the observation of bacteria, fungi and viruses.

The application history of SEM can be traced back to 1937 when Ardenne (Ardenne 1938) added scanning coils to a transmission electron microscope (TEM) and acquired the first scanning image. Zworykin et al. (1942) continued to develop the instrument and achieved a resolution of 50 nm. In the 1950s Oatley and his group in Cambridge manufactured the first commercial SEM-"Stereoscan" which was then released by Cambridge Scientific Instrument Company in 1965. There are more than seven SEM manufacturers in Europe, the US and Asia (e.g., FEI, Zeiss, JEOL and Hitachi), and more than 20,000 SEMs have been installed in the world (Amelinckx et al. 1997). Sub-nanometer resolution has been recently demonstrated in the state-of-the-art SEMs, for example, the FEI Verios (0.7 nm at 1 kV, released in 2012) (FEI 2012) and the Hitachi SU9000 (0.4 nm at 30 kV, released in 2011) (Hitachi 2011).

W. Han (✉)
Guangzhou, China
e-mail: Wei.Han@live.com

H. Jiao
Guangzhou, China
e-mail: huisheng.jiao@gmail.com

D. Fox
Trinity College Dublin, Dublin, Ireland
e-mail: Foxda@tcd.ie

R. Wang et al. (eds.), *Progress in Nanoscale Characterization and Manipulation*, Springer Tracts in Modern Physics 272,
https://doi.org/10.1007/978-981-13-0454-5_2

In this chapter, the principles and applications of SEM will be discussed with an emphasis on new progress of SEMs in nanoscale applications.

2 Fundamentals of the SEM

A modern scanning electron microscope consists of an electron optical system, a vacuum system, electronics system, computer and software. The electron optical system involves the formation of the electron probe, which includes the electron gun, the demagnification system (i.e. the condenser lens), the scanning unit, and the focusing system (i.e. the objective lens as sketched in Fig. 1). The electron-optical system produces a highly focused electron probe (∼1 nm) which is scanned in a raster over a region of the specimen surface. The interaction between the beam electron and the specimen generates a range of signals that can be collected by proper detectors equipped in the SEM to form images or spectra. The image can be displayed on a PC monitor simultaneously, while the SEM is scanning the electron probe on the sample surface. Usually we call the actual scan range horizontal field of view (HFW). If the width of monitor is L, then the magnification $M = L/\text{HFW}$. Since L is a constant, a higher magnification will be obtained if the scan area HFW is decreased.

The electron-optical system is crucial to the performance of the SEM, for example, the ultimate resolution relies on the quality of the electron gun and the probe. In this section, the components of the electron-optical system will be discussed in detail.

2.1 Electron Emitters

SEMs can be classified into thermionic and field-emission SEMs according to the methods used for electron emission. The tungsten cathode is now the dominant thermionic gun, while the LaB_6 filament is still being used by some SEM manu-

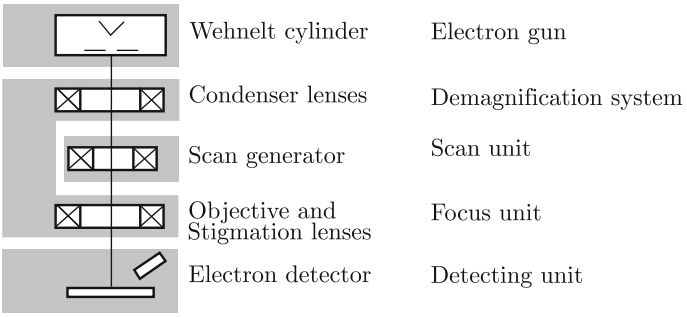

Fig. 1 Main structure of the optical column of the SEM

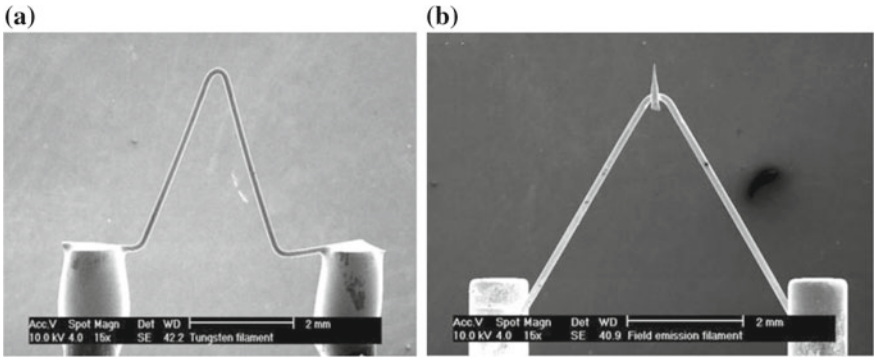

Fig. 2 SEM image of filaments of tungsten SEM (**a**) and FE-SEM (**b**)

facturers. Field-emission SEMs (FE-SEMs) have two variants: Schottky FE-SEM and cold FE-SEM, although strictly speaking Schottky field emission is indeed a field-assisted thermionic emission.

The filament of the tungsten SEM (W-SEM) is a hairpin-shaped tungsten wire with an apex diameter about 100 μm (see Fig. 2a). At high temperatures, the electrons in the tungsten wire gain enough kinetic energy and overcome the surface barrier so that an emission current is achieved. The emission current follows the Richardson-Dushman equation:

$$J = AT^2 e^{-B/T} \tag{1}$$

where A and B are constants. The typical resolution for tungsten thermionic gun SEMs is ~3.0 nm at 30 keV for the standard specimen (gold on carbon). The W-SEM is cheap and reliable, since it does not require ultra-high vacuum and the filament itself is inexpensive.

Figure 2b illustrates the typical morphology of the cold field emission emitter. A small piece of tungsten single crystal with an apex diameter of 10–100 nm is welded on the top of a hairpin-shaped tungsten wire. There are two anodes in the FE-SEM gun, i.e. extraction and acceleration anodes. A positive bias is applied on the extraction anode, which produces a strong electrical field at the adjacent area of the emitter tip due to the geometric field enhancement effect. The strong electrical field depresses the surface barriers and allows the electron to escape into the vacuum via the tunneling effect. The acceleration anode then accelerates the electron to its working energy, which may vary from a few tens of eV to tens of keV. The current density (A/m^2) is given by the following equation:

$$J = 1.54 \times \frac{10^{-10} E^2}{\varphi} \cdot \exp[-6.83 \times 10^9 \cdot \varphi^{3/2} \cdot k/E] \tag{2}$$

where E is the electric field at the emitter on the order of 10^9 V/m, φ is the work function and k is a constant. The current densities can reach 10^{12} A/m^2. The Schottky

Table 1 Comparison of three different emitters

Characteristics	W	Cold FE	Schottky FE
Brightness (A/cm^2 sr)	10^6	10^9	5×10^8
Energy spread (eV)	2	0.25–0.5	0.35–1.0
Cathode temperature (K)	2800	300	1800
Vacuum (Pa)	10^{-3}	10^{-8}	10^{-7}
Current stability	1%/1 h	5%/15 min	0.4%/1 h
Probe current	10 pA–2000 nA	1 pA–20 nA	1 pA–200 nA
Lifetime	100 h	>1 year	>1 year

emitter is a tungsten filament coated with ZrO_2. The ZrO_2 coating lowers the work function and in comparison to the cold FE emitter, the Schottky emitter is heated while it is working.

Table 1 lists the relevant characteristics of the electron emitters which can be used to evaluate their performance. Gun brightness is defined as the current density per solid angle. Since the brightness is invariant in the electron optics, the higher the brightness the larger the beam current can be acquired when a small probe is formed, which in turn regulates the signal to noise level and limits the demagnification of the probe. It can be seen that cold FE emitters offer the highest brightness. Energy spread in the electron probe can affect the probe size through the chromatic effect, so a small energy spread is in favor of small probe size. The energy spread of the field emission emitters is an order of magnitude smaller than that of the thermionic gun. The advantages of W-SEM (thermionic emitters) are however large probe current, cost efficiency, and less-demanding maintenance.

The operation of the cold FE emitter requires ultrahigh vacuum in the gun chamber. The residual gases in the gun chamber will nevertheless contaminate the filament tip gradually under the working conditions, and the emission will fluctuate from time to time due to the contamination. After several hours the emitter must be flashed at a high temperature to burn out the contaminant. This instability has limited the application of cold FE SEMs. For example, on-line instruments in semiconductor industry usually don't choose cold FE emitter. The probe current of the cold FE emitter is also lower than that of the Schottky FE emitter, so the cold FE SEM is less suitable for many applications which need higher and more stable currents, such as electron back scatter diffraction (EBSD), wavelength dispersive X-ray analysis (WDX), low vacuum or in situ dynamic applications. Schottky emitters can however meet the requirements of these techniques. Moreover, recent developments have improved the performance of the Schottky emitter to a level close to that of the cold FE emitter in terms of resolution and energy spread. A resolution of 0.7 nm and an energy spread less than 0.2 eV at 1 kV was achieved in the FEI Verios XHR SEM (Schottky Gun) which is equipped with a monochromator.

2.2 Electron-Optical Column in SEM and Probe Formation

The electron passes through the column of the SEM and the electron beam is demagnified by the condenser lens and focused by the objective lens to form a fine electron probe on the specimen surface. The finer the probe, the better the spatial resolution. The probe size is determined by the quality of the lenses and limited by the wave nature of the electron beam as well as the brightness of the gun. For accelerating voltages from 5 kV to 30 kV, the probe size can be calculated by the following equation (Smith 1972):

$$d = (C_s^{1/4}\lambda^{3/4})\left[1 + \frac{I_b}{\beta\lambda^2}\right]^{3/8} \tag{3}$$

where C_s is the spherical aberration coefficient of the objective lens, λ the wavelength of electrons, β the brightness of the electron gun and I_b the beam current. For a tungsten cathode thermionic gun, the brightness is about 10^5 A cm^{-2} sr^{-1}, and the image performance is not determined by the lens but by the electron gun. For FE-SEM gun the brightness is about 10^8 A cm^{-2} sr^{-1} (Goldstein et al. 1992a), the probe size is limited by the performance of the lens (Amelinckx et al. 1997). For normal FE-SEM 1–2 nm probe can be acquired, while the energy spread must be considered at low accelerating voltages (<5 kV) because of severe chromatic aberration. The size of the probe also increases with increasing beam current, since the statistical coulomb interactions at the beam crossover can modify the lateral velocities of the electrons known as the Boersch effect.

The lenses used in SEM are electromagnetic lenses, except the gun lens which is an electrostatic lens. To meet the requirements of nanoscale applications the modern lens system is designed in combination with the detector system. For the objective lens system there are mainly two types of lenses: the out-of-lens (field-free) type and the in-lens (immersion) type objective lens. For a field-free lens, the sample is placed below the pole piece of the objective lens. When decreasing the working distance the detector efficiency will be decreased. Most high resolution SEMs use this type of objective lens. In the immersion objective lens, the sample is placed in the gap between the upper and lower pole pieces of the lens. The advantage is that a very short working distance can be applied, while the detector efficiency is still quite high with an in-lens detector. This is an effective way to increase resolution in the low kV range due to the decrease in spherical and chromatic aberration. In most ultra-high-resolution SEMs immersion objective lenses are equipped as the standard. However, the magnetic field of the lens could be influenced by magnetic samples, producing stronger astigmatism. Another problem is that it may influence the trace of BSE and induce bending Kikuchi band in EBSD analysis. In commercial SEMs some suppliers combine these two lens types into one system as illustrated in Fig. 3. Two operation modes can be switched freely, alllowing these problems to be overcome. More details on this subject can be found in dedicated book (Zhou and Wang 2007).

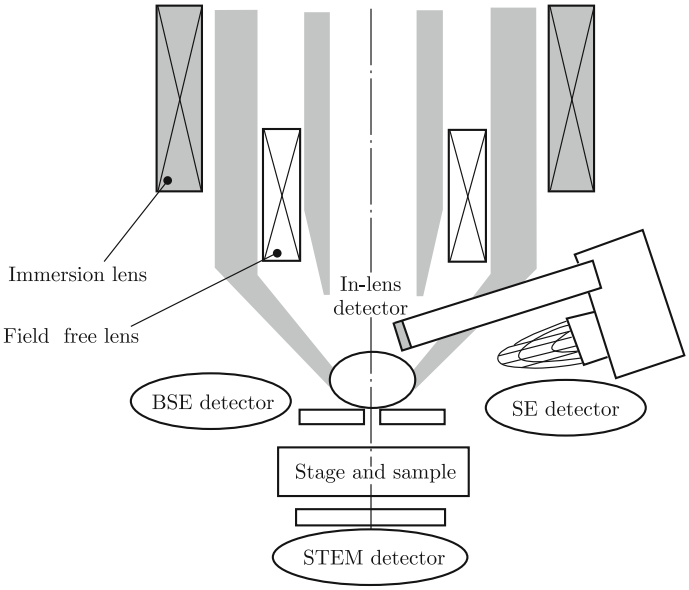

Fig. 3 Illustration of objective lens and detectors in modern SEM system

2.3 Signal Generation and Detection

During the interaction of the electron beam with the specimen, the beam will penetrate into the specimen ranging from several nanometers to several micrometers depending on the energy of the incident electron and the materials. In this process the incident electrons are randomly scattered. Both elastic and inelastic scattering will happen. The scattered electrons form an interaction volume with a water-drop shape inside the specimen. Various signals can be generated in the interaction volume and some of them will escape from the sample and be collected by the detectors. This process is illustrated in Fig. 4. These signals include secondary electrons (SE), backscattered electrons (BSE), Auger electrons, X-rays (including characteristic X-rays and Bremstrahlung X-rays), and cathodoluminescence (CL). The signals carry some information of the specimen. Among them SEs and BSEs are the most widely utilized signals because SEs can offer very high resolution images and BSEs can provide compositional information. In this section, we will discuss SEs and BSEs, while the X-ray and the analytical capabilities of SEM will be introduced in the next section.

The Interaction Volume: The resolution of SEM is not only dependent on the primary beam size, but also the interaction volume. The size of the interaction volume is determined by the beam energy, the specimen, and the incidence angle. According to Monte Carlo simulation with the same incident beam energy (15 kV), the beam will penetrate into bulk WSi_2 for 1.2 μm in depth, while it will penetrate into bulk KCl for

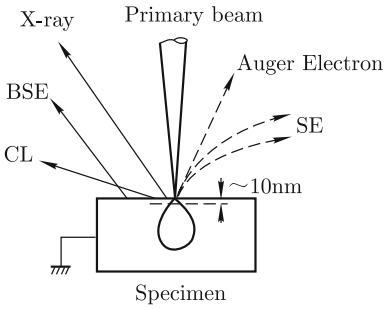

Fig. 4 Signals from the interaction of electron beam and specimen

4.8 μm in depth. The interaction volume has a strong Z effect. Samples with higher atomic number Z have smaller interaction volumes. Another influencing factor on the interaction volume is the beam energy. Smaller incident beam energy corresponds to reduced interaction volume and penetration depth. In Fig. 5 two images with different accelerating voltages are obtained on a fractured aluminum specimen at 5 keV and 20 keV, respectively. The 5 keV image shows surface details quite clearly, while some information is hidden in the 20 keV image.

In nanoscale research the small interaction volume will be more important. That means low kV performance is very important for nanoscale applications. However, low kV imaging typically has larger beam sizes and higher energy spread. Fortunately technical progress in SEM has overcome these problems in the low kV range. Another advantage comes from the fact that many nano-materials are non-conductive, at low kV the interaction volume is small therefore the yield of SEs will be increased accordingly. This effect can be exploited to balance the rate of electrons entering and exiting the sample, thereby mitigating the charging effect.

Signal Generation: As a result of the elastic interaction, the beam electron may be backscattered into the vacuum with a maximum energy equal to the primary electron energy. Inelastic interaction between the beam electron and the specimen can result in ionization of the specimen atoms, which produces secondary electrons throughout the total interaction volume. These secondary electrons have an average energy of 2–6 eV and may escape from the specimen from a small depth of about 1 nm for metals, and of the order of 10 nm for carbon. The spectrum of all electrons coming out of a specimen when it is irradiated with an electron beam of energy E_{PE} is shown in Fig. 6. By convention the electrons with an energy below 50 eV are called secondary electrons (SE) and the others are the backscattered electrons (BSE).

It should be noted that a backscattered electron generated deep in the material is energetic enough to produce secondary electrons on its way back to the surface. This type of SE is called SE2, while the secondary electrons generated by the primary beam are called SE1. If a backscattered electron hits the chamber or the pole piece of the electron microscope, some secondary electrons are produced and called SE3. Usually SE1 carries high resolution information, while SE2 and SE3 generate low resolution

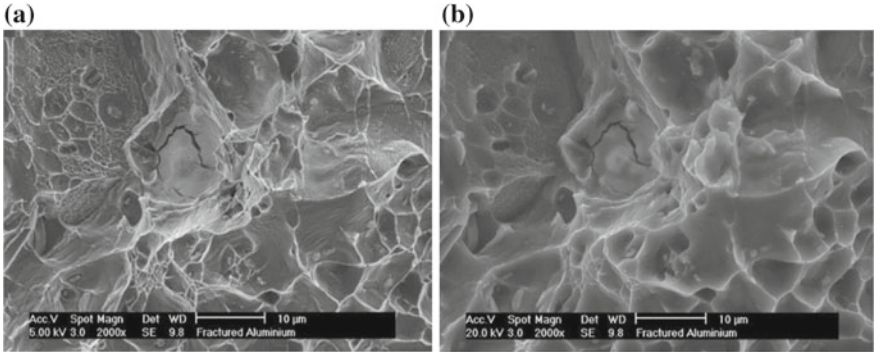

Fig. 5 A sample of fractured aluminum that has inclusions of copper, SE images at 5 keV (**a**) and 20 keV (**b**)

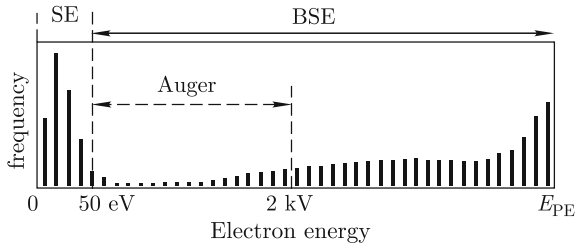

Fig. 6 Energy distribution of electron signals

background. In terms of the detection, it is however not possible to separate SE1, SE2 and SE3, while specific detector configuration may depress the contributions of SE2 and SE3, for example the in-lens (or through lens) detectors.

SE images can generally be easily interpreted as the topographical illustration of the sample surface without any special knowledge. As the beam scans along the surface of the sample, the angle of incidence changes due to the variation in the local roughness of the sample surface. The number of electrons leaving (and therefore being detected) depends on the angle of incidence, which is fundamental for the formation of the topographical contrast. Edges, which have a high angle relative to the incident beam, will produce many SEs compared to the flatter surrounding areas. This bright edge area is referred to as the "edge effect". As shown in Fig. 7, secondary electron images also exhibit a large depth of focus and the image has stereoscopic effects due to shadow effect. The resolution is higher in comparison to the BSE image.

The most widely used SE detector in SEM is the Everhart-Thornley detector (Everhart and Thornley 1960), which is a scintillator-photomultiplier system. About 10 kV positive potential is used on the scintillator to accelerate secondary electrons. A Faraday cage made of copper mesh is used to cover the scintillator. The bias on the cage can be varied from −100 V to +250 V. If +250 V is used on the cage secondary electrons will be attracted to the cage. If −100 V is used secondary electrons will be

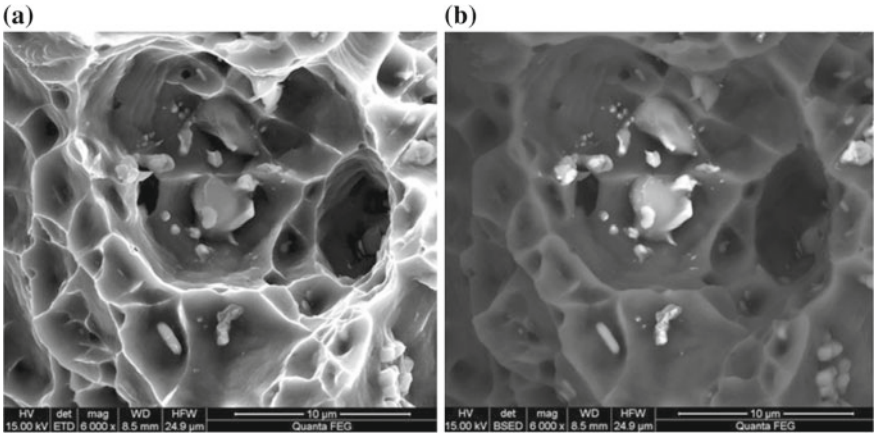

Fig. 7 Comparison of SE image (**a**) and BSE image (**b**) of Al fracture in the same field of view

repelled from the Faraday cage, in which case only BSE can be detected. Usually the SE detector is placed inside the specimen chamber above the final lens plane. In high resolution SEM another in-lens SE detector will be installed inside the objective lens or above it.

In Fig. 6, the large peak around the primary beam energy results from the Rutherford scattering and this process increases with increasing atomic number Z. Therefore, the number of BSEs coming out of the specimen reflects the average Z value of the material. This is the most important contrast mechanism for the backscattered electrons. The right image in Fig. 7 illustrates some features of BSE images. The resolution of the BSE image is not as good as that of the SE image. The image also looks somewhat transparent because the energy of BSE is large enough to escape from up to one third of the total interaction depth. Another feature is the Z-contrast, i.e., the material in the bright areas has higher atomic number than that of other areas.

The yield of BSE increases from 0.05 for carbon to 0.5 for gold. During the scattering process BSE can go any direction. It is difficult to collect BSE with high efficiency because the energy of the BSE is too high to be attracted by high positive potential. BSE detectors are typically placed under the pole piece of the objective lens to increase the collection angle. BSE outside this angle cannot be utilized for signal. Although the yield of BSE is higher than that of SE, the efficiency of BSE detection is much less than that of the SE detection. Another limitation is that the resolution of the BSE image is worse than that of the SE image because of the larger escape depth. No matter how small the actual diameter of the primary beam the interaction volume will degrade the resolution of the BSE image.

The solid state BSE detector (SS-BSD) is the most common BSE detector on the market. It is basically a diode that amplifies the high energy BSE striking the detector, as illustrated in Fig. 8. When a BSE strikes the detector, electrons in the material move from the valence to the conduction band leaving holes in the valence

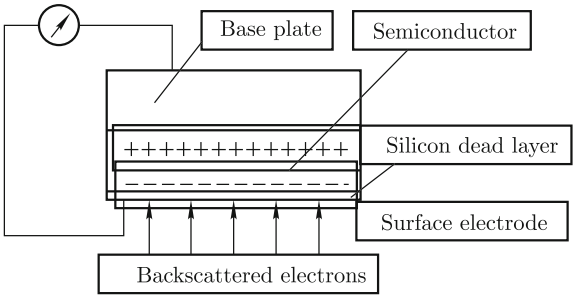

Fig. 8 Structure of solid state BSE detector

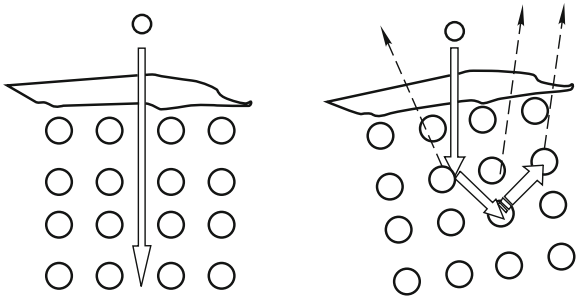

Fig. 9 Schematic illustration of electron channeling effect, in the left figure channeling happens at a particular incidence direction to the crystal. In the right figure there is no channeling effect at random incidence direction

band. If a potential is applied, the e^- and h^+ can be separated and collected, and the current can be measured. The current is proportional to the number of BSEs that hits the detector.

The SS-BSD is usually divided into two detection areas. This will allow for either topographical or elemental imaging of BSE by subtraction or addition signals from two parts respectively. Some BSD systems even separate the SS-BSD into 4 or 5 segments. More combination modes have been developed to meet the requirement of different applications.

In addition to the material contrast, more information about the specimen is necessary to interpret BSE images, especially for crystalline materials where the contrast of BSE image is related to crystal orientation (so called the channeling effect) as well, as shown in Fig. 9. This channeling effect has been utilized for characterization of crystalline materials. Commercially available detectors have been developed for SEM. This instrument is called EBSD. Applications of EBSD will be discussed in detail in the next section.

BSE signal is indispensable due to its material contrast, for example in the steel industry BSE signal is used for finding inclusions in steels. In forensic science BSE signal is an essential detector for the investigation of gunshot residue (GSR) (ASTM E1588-07 2007; Andrasko and Maehly 1977). In the natural resources area the BSE signal is used for investigating valuable minerals. In the above applications BSE signals can supply a rough distribution of sample composition. In biological samples BSE imaging is now a unique way to analyze resin embedded slices or cross-sections milled by focused ion beam (Knott et al. 2008; Li et al. 2013).

3 Analytical Capabilities of the SEM

SEM provides a platform to characterize the microstructure of materials. However, with only high resolution images and no analytical capabilities it is difficult to comprehensively characterize the microstructures. Since many different signals are generated when a beam of electrons bombard the surface of a specimen, chemical and crystal information can be acquired through the use of the appropriate detectors. The energy dispersive X-ray spectrometer (EDS) is one of the most useful systems for micro-chemical analysis in SEM. An electron backscatter diffraction (EBSD) system is often used for crystal and orientation measurements in SEM. In the following chapters these techniques will be presented in detail.

3.1 X-Ray Microanalysis and Nanoanalysis

1. Generation of X-rays in SEM

In a SEM chamber, a beam of high energy electrons bombards the surface of samples. When an electron with high energy interacts with an atom in samples it may result in the ejection of an electron from an inner electron shell. This will leave a vacancy in this shell and the atom is in an excited state. The excited atom is unstable and an electron from an outer shell fills the vacancy. Electrons in different shells have different energy and the minimum energy required to remove an electron from a particular energy level is known as the critical ionization energy E_c or X-ray absorption edge energy. The critical energy has a specific value for any given energy level and is typically referred to as the K, L or M absorption edge. The change in energy during the de-excitation or "characteristic energy" is determined by the electronic structure of the atom which is unique to the element.

There are two approaches to release this "characteristic" energy. One is the emission of an X-ray photon (fluorescence yield = w) with a characteristic energy related to the energy of different electron shells of an atom. The second way is by releasing so called Auger electrons (Auger yield = a).

The probabilities of energy release by these two ways can be written as:

$$a + w = 1 \tag{4}$$

For any given shell, the probability of X-ray emission is relative small for light elements. For example, the value of w for the Si K shell is 0.047, Co K shell is 0.381 and 0.764 for the Mo K shell.

If a vacancy is in the K shell of an atom, X-ray emission from de-excitation is called the K line. Similarly, X-ray emission from de-excitation due to a vacancy in the L or M shell is called the L line or M line. Furthermore, if an electron from the L shell fills the K shell vacancy, the X-ray emitted in this transition is termed the K_α line. If an electron from the M shell fills this vacancy the X-ray emitted in this

transition is termed the K_β line. The K shell is the closest shell to the nucleus, it therefore requires the most energy to remove electrons from this shell. The K line has the highest energy if an atom has K, L and M lines.

The intensity of a given line primarily depends on the probability of X-ray generation as a result of a given transition. The relative probability of generating X-rays at the various ionization energies for a given element depends on the value of the incident energy and the excitation cross section for the relevant shell. The cross section itself can be expressed in terms of the overvoltage, U ($U = 2 \sim 3$, gives the highest probability for X-ray generation), which is simply the incident beam energy divided by the critical ionization energy for a particular shell.

2. EDS System for Microanalysis

EDS systems are commonly used on SEM for micro chemical analysis. An EDS system is composed of three basic components: (1) X-ray detector, which detects and converts X-rays into electronic signals. (2) pulse processor, which measures the electronic signals to determine the energy of each X-ray detected and (3) analyzer, which displays and interprets the X-ray data.

Figure 10 shows a diagram of an old Si (Li) EDS detector. This is a typical Si(Li) detector and a modern EDS detector still uses this configuration except the liquid nitrogen Dewar for cooling the crystal. In an EDS detector, the core component is crystal, which is a semiconductor device, often made of Si, converting X-ray photons into electric charges. These charges are transferred to a field effect transistor (FET) just behind the crystal and converted to voltage output. In front of the crystal, a thin window made of Be or polymer seals the crystal from outside. A Be window is robust but heavily absorbs low energy X-rays. That means only X-rays from elements above Na can be detected. Nowadays EDS detectors on SEMs all use ultra-thin polymer windows. This enables the detection of X-rays down to less than 100 eV (Be). These ultra-thin polymer films are supported on a silicon grid to withstand the pressure difference between the detector vacuum and a vented microscope chamber at atmospheric pressure. An electron trap made of permanent magnets is placed in front of the window to keep electrons away from the crystal. Electrons could cause serious background artifacts. At the beginning of the detector there is a collimator which ensures that only X-rays from the area being excited by the electron beam are detected and stray X-rays from other parts of the microscope chamber are not included in the analysis.

During the last few decades the crystal in the EDS detector has experienced a revolution. Si (Li) was the first material used in EDS detectors and remained the most common choice until the first decade of 21st century. The most common crystal is Si, into which is drifted lithium (Li) to compensate for small levels of impurity. The modern EDS system uses the Silicon drift detector (SDD) which was first manufactured in the 1980s for radiation physics. The development of this detector, and advances in its fabrication methods, have led to a liquid nitrogen free EDS detector to replace the Si (Li) detector with better performance and productivity in SEM. Figure 11 shows the difference between these two types of detectors.

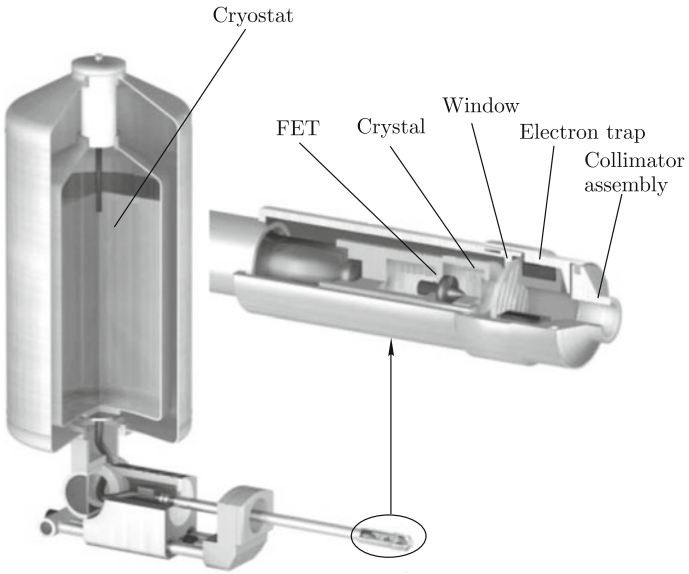

Fig. 10 Diagram showing components in a Si (Li) EDS detector (Oxford 2002)

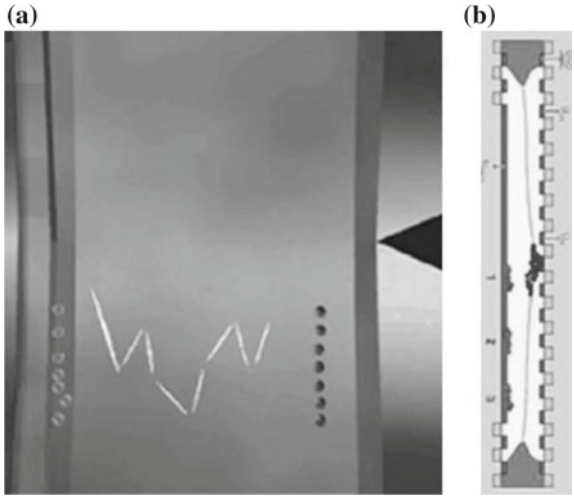

Fig. 11 Cross section of X-ray detectors. Diagram showing generation of electron-vacancy pairs in a traditional Si (Li) crystal (**a**) and in a SDD crystal (**b**) (Ketek 2013)

Normally a Si (Li) crystal is about a 3 mm thick disc and an SDD crystal is only about 500 μm in thickness. Also, the anode in an SDD crystal is reduced to about 50 μm in diameter for charge collection. In an SDD crystal a negative bias is applied to both sides of the disc. But on one side of the planar structure the bias is graduated across the device by means of a series of 'drift rings' such that a strong transverse electric field component is developed within the structure. This is used to direct

electrons produced as a result of X-ray interactions towards a small anode. On the opposite side of the device (X-ray entrance side) there is a uniform shallow implanted junction contact to allow good low-energy X-ray sensitivity and minimum charge loss. This drift detector structure has very low capacitance which provides excellent energy resolution at relatively short electronic processing times and also allows operation at very high count rates (Oxford 2012). SDD detectors clearly possess an important advantage because they maintain best resolution performance at much higher count rates than Si (Li). Higher productivity is achieved by collecting data faster with no loss of analytical performance.

3. Qualitative and quantitative EDS analysis

EDS analysis in SEM is one of the most convenient techniques for obtaining chemical information of interesting features. It gets not only elemental information but also the weight and atomic percent of ingredients and it is one of the most accurate methods for composition analysis on the micron or nano level. In general, the detection limits of SEM EDS reach 0.1 wt.% level, and even hundreds of ppm for heavy elements (Goldstein et al. 1992b). It is well known that electron probe microanalysis (EPMA) is considered as the most accurate technique for quantitative composition analysis. However with the progress of the EDS technique both in hardware and software, recent experiments have revealed that the SDD EDS could give very high quality data, which is comparable with EPMA.

Micro chemical characterization of SEM EDS analysis falls into two categories: (a) qualitatively to determine the element species and their distribution, and (b) quantitatively obtain the concentrations of each element. For most systems, as shown in Fig. 12, elements with obvious peaks in an EDS X-ray spectrum can be identified correctly. However, if two or more element peaks are close to each other or a minor peak is not obvious, it will be difficult to identify the peak correctly. An important specification for characterizing performance of an EDS system is its ability to resolve peak overlaps, termed as energy resolution. Resolution is quoted as the full width at half maximum (FWHM), normally using FWHM of the X-rays of the manganese (Mn) K_α line (Mn K_α). This is convenient for manufacturers of EDS detectors, because they can use a Mn K_α emitting ^{55}Fe radioactive source to monitor individual sensor and detector performance without the need of an SEM. The lower the number the better the resolution a detector has and the better it will be at resolving peaks due to closely spaced X-ray lines. Currently, the energy resolution of a modern SEM SDD is in the range of 120–130 eV for Mn K_α.

If there are peak overlaps or minor peaks in an EDS spectrum, manual peak identification is always needed for element confirmation. Commercial software always provides special tools, such as spectrum simulation based on identified elements, to check for any possible overlaps or minor elements. For minor peaks, in order to identify the element without doubt, an effective approach is to acquire more counts by elongating the acquisition time to make these peaks more obvious. EDS analysis therefore benefits from SDD detectors due to their enhanced energy resolution and 10 times higher count rate than Si (Li) detectors (Fig. 13).

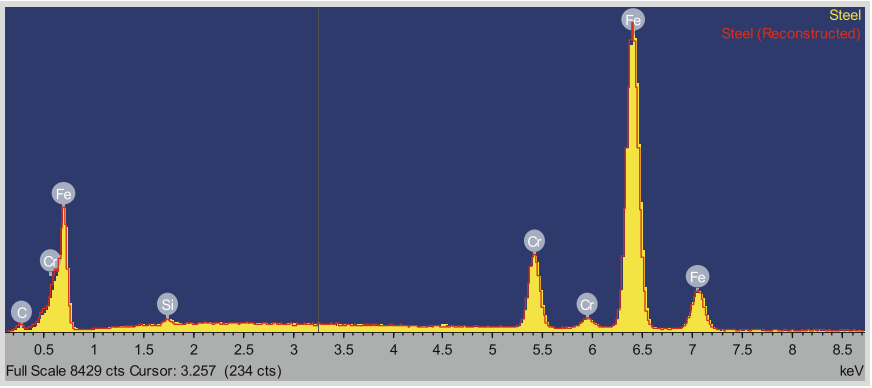

Fig. 12 Comparison between simulated spectrum (red line) and acquired spectrum

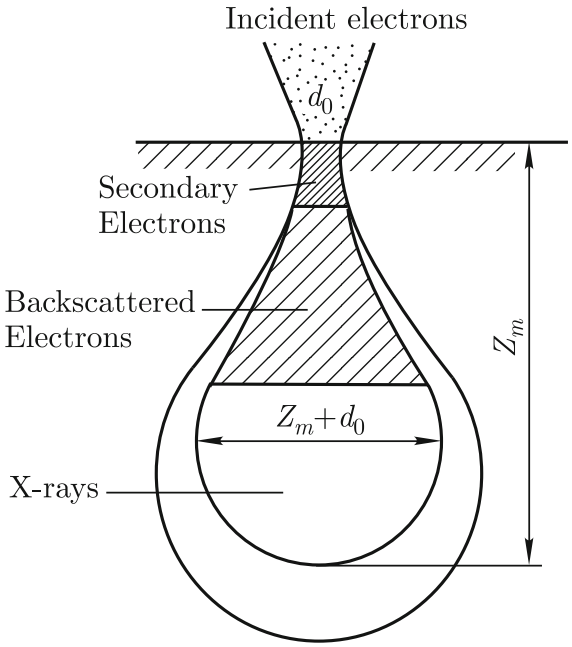

Fig. 13 Diagram showing the interactive volume of electron beam and a sample (Reimer 1979)

After the elements have been identified, quantitative analysis may be needed to give the concentration of each element. This requires the accurate measurement of the peak intensities. As there is a contribution from a non-linear background over the entire energy range, a 'top-hat' filtering method is one of the best algorithms to suppress the background. The peak intensities are then obtained using a least squares fitting routine. Once these intensities have been determined matrix corrections (i.e. XPP correction) are applied to determine the concentration of each element. XPP has favorable performance for situations of severe absorption such as

Table 2 Quantitative analysis of two EDS standards

Anorthoclase			Benitoite		
Element	wt. %	Certificate	Element	wt. %	Certificate
O	46.84	46.54	O	34.49	34.83
Na	2.69	2.75	Si	19.78	20.37
Al	10.07	10.53	Ti	12.02	11.57
Si	30.65	30.06	Ba	33.71	33.21
K	9.57	9.46			
Ca	0.17	0.17			

the analysis of light elements in a heavy matrix and for samples that are tilted with respect to the incident electron beam. Table 2 gives the quantitative analysis of two samples with certified concentration showing the accuracy of modern EDS analysis. From Table 2 it is seen that the EDS gives very accurate measurements in comparison with the certified concentration, even for the light element oxygen and minor elements with concentration as low as 0.17%.

4. Spectrum mapping and spatial resolution

For an unknown sample spectrum mapping is the most efficient way to learn about the sample. A field on the sample is defined and then the X-ray spectrum map performs the simultaneous acquisition of X-ray data for all possible elements from each pixel on this area. Beam dwelling time per pixel and the number of frames can be set for spectrum map acquisition in SEM. In a spectrum map each pixel is associated with a single spectrum, it is therefore possible to display a map of any element from stored data without the need to define the element list before acquisition. It is also easy to reconstruct spectra, linescans or maps after acquisition. Element maps can be used to quickly highlight compositional variations in a sample.

The spatial resolution of an element map depends on the interaction volume between the electron beam and the sample. The overall dimensions of the interaction volume depend strongly on the incident beam energy, since the cross section of elastic scattering follows an inverse square dependence with the electron beam energy. As the beam energy of the incident electrons increases, they are able to travel further into the sample. An additional factor which affects the overall dimensions of the interaction volume is the rate at which electrons lose energy. The rate of energy loss is inversely proportional to the energy of the electron. This means that with an increase in electron beam energy, the rate at which these electrons lose energy decreases, such that they are able to travel further into the sample. The shape of the interaction volume depends strongly on the atomic number of the material. The cross section for elastic scattering is proportional to the square of the atomic number of the material. This means that for a fixed beam energy, electrons entering a high

atomic number material will be scattered away from their original directions, giving the volume "width" and reducing penetration into the material. However, in a low atomic number material, electrons will penetrate into the sample much deeper, losing energy as they undergo inelastic scattering events, until the energy of the electrons is such that the probability of elastic scattering begins to dominate. This gives rise to the shape of the so called "pear shaped" volume. Eventually, the electrons do not have sufficient energy to scatter further into the sample, which corresponds to the "boundaries" of the electron interaction volume.

$$Z_m = 0.033 \cdot (V_0^{1.7} - V_k^{1.7}) \cdot A/\rho Z \tag{5}$$

where Z is the atomic number, V_0 is the accelerating voltage (kV), V_k is the excitation energy (kV), A is the atomic weight and ρ is the density of the sample (g/cm^3).

The interaction of the electron beam with the sample is complex, where a whole host of interaction and scattering events are possible. The Monte Carlo method is a mathematical technique, which attempts to model the shape of the interaction volume by simulating a large number of electron trajectories through the solid materials (Joy 1995). Figure 14 shows the interaction volume in bulk Ni at different beam energies.

It clearly shows that the interaction volume decreases when the beam energy decreases. The spatial resolution of element maps will be significantly improved when beam energy is changed from 20 kV to 5 kV due to the smaller interaction volume. As the accelerating voltage increases, the interaction volume excited within the sample increases. It means that both X-rays and backscattered electrons can be generated much deeper, affecting both imaging and analysis. Figure 15 shows Ni, Cr and Nb overlapped map under 20 and 5 kV. Obviously, low kV will give an element map with better resolution because of the shallow penetration of electron beam and small interaction volume.

To achieve better spatial resolution, low kV should be used for elemental mapping. However, low kV and small interaction volume mean less X-ray signals generated. In order to collect X-ray maps with moderate statistics, spectra collection may take tens of minutes or even hours. Recently, large size SDD detectors (up to 150 mm^2 active area) were fabricated which can collect more X-rays under the same SEM operating conditions. For comparison, the active area of a crystal in commonly used EDS detectors is in the range of 10–30 mm^2. With these large area SDD detectors, X-ray maps with a resolution of tens of nanometers can be achieved,

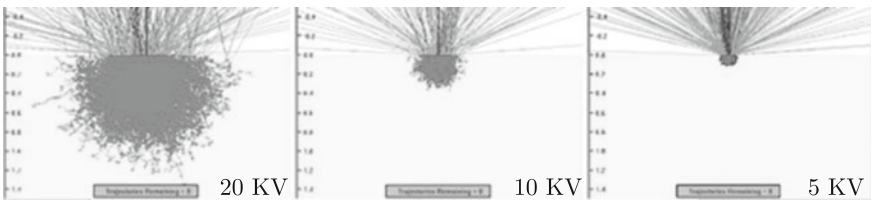

Fig. 14 Monte Carlo simulation of the interaction volume in Ni with different beam energy

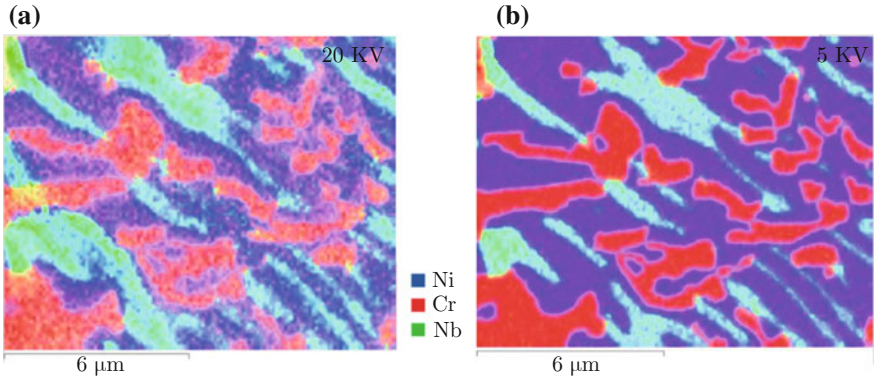

Fig. 15 Overlapped Ni, Cr and Nb map showing the better spatial resolution at low kV

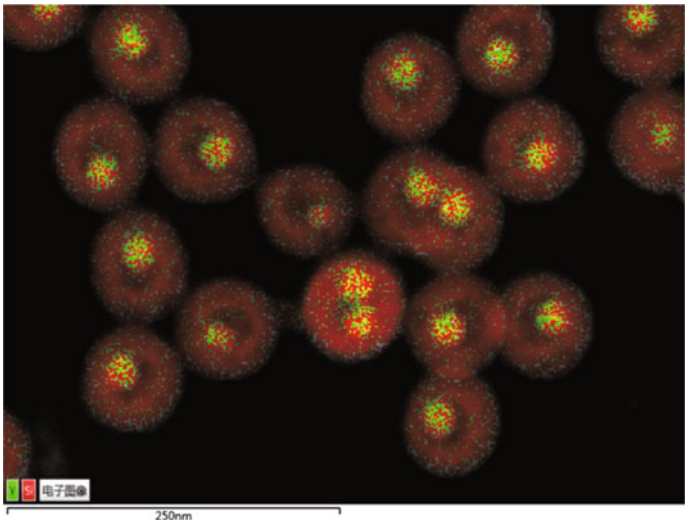

Fig. 16 High spatial resolution element mapping shows the distribution of Si and Y in core/shell nanoballs. The diameter of the balls is about 80 nm. Image courtesy of Wu. W

as shown in Fig. 16. For nanoscale element X-ray mapping, the accelerating voltage is low. The performance of SDD detectors at low energy, such as energy resolution and sensitivity, becomes more important. When small features <1 μm in size are being analyzed, the beam voltage needs to be reduced to avoid generation of X-rays from surrounding material. However, at low kV only low energy lines are available for analysis and X-ray lines are closer together at low energy. Fortunately, excellent low energy resolution is already achieved with very large sensor sizes to maximize count rate and peak sensitivity under low kV operating conditions or when analyzing beam sensitive samples.

3.2 Wavelength Dispersive X-Ray Spectrometry in SEM

As well as an EDS system, a wavelength dispersive X-ray spectrometer (WDS) can also be fitted onto an SEM chamber for chemical analysis by collecting X-rays generated by the electron beam. Data collection and analysis with EDS is a relatively quick and simple process because the complete spectrum of energies is acquired simultaneously. However, using a WDS, the spectrum is acquired sequentially as the full wavelength range is scanned. Although it takes longer to acquire a full spectrum, the WDS technique has much improved energy resolution compared to EDS. Typical energy resolution of an EDS detector is 70–130 eV (depending on the element), whereas peak widths in WDS are 2–20 eV. The combination of better resolution and the ability to deal with higher count rates typically allows WDS to detect elements at an order of magnitude lower concentration than EDS.

The development of WD spectrometers goes back long before EDS detectors. The first electron probe microanalyzer (EPMA) was developed during the 1940s and used an optical microscope to observe the position and focus the electron beam on the sample. Later, WDS spectrometers were fitted to SEMs, which allowed the specimen to be positioned more precisely under the electron beam and also made possible a visual picture of the distribution of a chosen element—the X-ray map.

In addition to an EDS detector, the WDS spectrometer can also be fitted on a port of the SEM, usually at an angle inclined to the horizontal so that it provides an identical X-ray take off angle to the EDS detector. Although the WDS technique often requires a higher SEM beam current than that typically used for EDS, the X-ray data is usually acquired from EDS and WDS simultaneously. If the EDS detector is fitted with a variable collimator there is no compromise in performance for either technique.

1. Components in WDS and working principle

Inside the spectrometer, analyzing crystals of specific lattice spacing are used to diffract the characteristic X-rays from the sample into the detector (Fig. 17). The wavelength of the X-rays diffracted into the detector may be selected by varying the position of the analyzing crystal with respect to the sample, according to Bragg's law ($n\lambda = 2d \sin\theta$), where n is an integer referring to the order of the reflection, λ is the wavelength of the characteristic X-ray, d is the lattice spacing of the diffracting material, and θ is the angle between the X-ray and the diffractor's surface. A diffracted beam occurs only when this condition is met and therefore interference from peaks of other elements in the sample is inherently reduced. However, X-rays from only one element at a time may be measured on the spectrometer and the position of the crystal must be changed to tune to another element.

The wavelength dispersive spectrometer consists of two major components-the analyzing crystal and the proportional X-ray detector. The spectrometer shown in Fig. 18 is of the fully focusing, or Johansson type, where the crystal, the X-ray source,

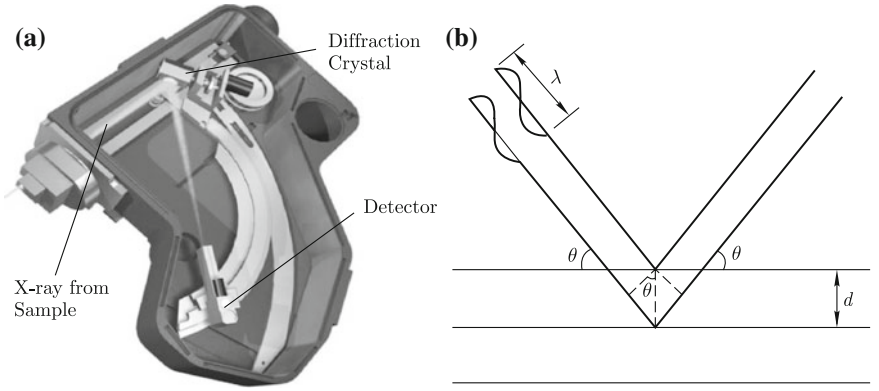

Fig. 17 Components inside a WDS spectrometer (**a**) and diagram of Bragg's law (**b**) (Oxford 2004)

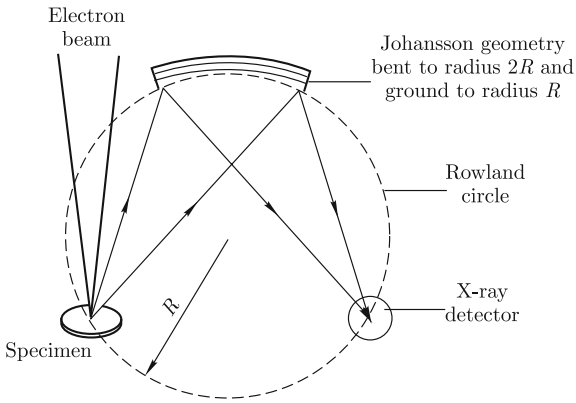

Fig. 18 Diagram of a fully focusing geometry for a WDS (Oxford 2004)

the sample, and the detector all remain on a circle of constant radius. This circle is known as the Rowland circle. The crystal planes are bent to twice the radius of the Rowland circle, and the crystal itself is ground to the radius of the circle. The crystal moves along a screwed rod in a linear fashion, simultaneously rotating through an angle θ. To maintain the fully focusing geometry, the detector moves through an angle of 2θ.

The spectrometer in Fig. 18 is known as a fully focusing linear type. The second type of crystal geometry is not fully focusing, known as Johann geometry, in which the diffracting crystal is bent to a radius of $2R$ and only part of the X-rays can be diffracted into the detector. In either crystal geometry the output of the detector is connected to an amplifier where it is converted to a voltage pulse which is then counted or displayed on a rate meter.

In a commercial WDS mechanical limitations make it impractical for one analyzing crystal to cover the entire elemental range. To cover the range of elements that need to be detected, a range of crystals is offered in a wavelength spectrome-

ter. Crystals of larger *d* spacing are used to diffract the longer wavelengths from the lighter elements. Pseudo crystals have been developed for these light elements, and are known collectively as layered synthetic microstructure (LSM) crystals. The LSM crystals are available in a range of different *d* spacings (e.g. 6, 8 and 20 nm), optimized for different elements. Other crystals commonly used for X-rays with short wavelengths from heavy elements are LiF (Lithium Fluoride), cleaved along either (200) or (220) plane, TAP (Thallium acid phthalate) and PET (Pentaerythritol).

Detectors used in WDS are usually of the gas proportional counter type. Generally, X-ray photons are diffracted into the detector through a collimator (receiving slit), entering the counter through a thin window. They are then absorbed by atoms of the counter gas. A photoelectron is ejected from each atom absorbing an X-ray. The photoelectrons are accelerated to the central wire causing further ionization events in the gas, so that an "avalanche" of electrons drawn to the wire produces an electrical pulse. The detector potential is set so that the amplitude of this pulse is proportional to the energy of the X-ray photon that started the process. Electrical pulse height analysis is subsequently performed on the pulses to filter out noise. There are two types of gas proportional counters: sealed counter (SPC) (usually xenon or a xenon-CO_2 mixture) and gas flow counter (FPC) (usually P-10: argon with 10% methane). Generally, SPCs are used for high-energy X-ray lines, while FPCs are used for low energy X-ray lines.

To maintain the correct geometrical relationship between specimen, crystal and detector for the full range of diffracted angles, it is necessary to maintain all three on the Rowland circle. To analyze a particular element it is important that the crystal and detector are positioned accurately and associated counting electronics are set up correctly. In the past this was a tedious and complex procedure, but automation and PC control have made WDS operation very straightforward, routine and reliable.

Using EDS, all of the energies of the characteristic X-rays incident on the detector are measured simultaneously and data acquisition is therefore very rapid across the entire spectrum. However, the resolution of an EDS detector is considerably worse than that of a WDS spectrometer. The WDS spectrometer can acquire the high count rate of X-rays produced at high beam currents, because it measures a single wavelength at a time. This is important for trace element analysis. For EDS detector, situations may arise in which overlap of adjacent peaks becomes a problem. Many of the overlaps can be handled through deconvolution of the peaks. Others, however, are more difficult, particularly if there is only a small amount of one of the overlapped elements. An example of the difficult overlap situation is shown in Fig. 19. In this figure, Si K lines are overlapped with W M lines in the EDS spectrum, but with WDS, different lines from two elements are clearly separated. In practice it is advantageous to use the speed of EDS for an initial survey of an unknown sample because major elements will be rapidly identified. However, if trace elements are present they will not be identified, and it may be difficult to interpret complex overlaps. Following the initial EDS survey, WDS can be used to check for overlaps and to increase sensitivity for trace elements.

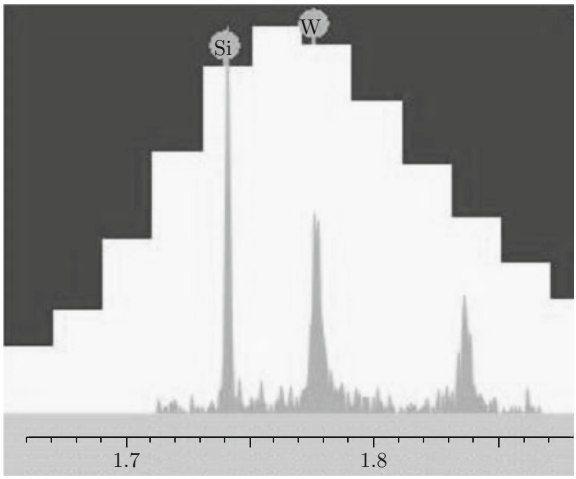

Fig. 19 Overlapped Si and W X-ray peak in EDS but separated in WDS scan

2. New parallel beam WDS

In addition to the WDS described in previous section, a new type of WDS, called parallel beam WDS, was developed recently, as shown in Fig. 20. Conventional WDS uses curved crystals to disperse and focus the X-rays onto a detector. Parallel beam WDS collects a large solid angle of X-rays diverging from the sample and re-directs them into a parallel beam incident on various flat diffracting crystal and then into a detector. Normally, parallel beam WDS systems are optimized for only one or two elements for each diffractor and a single WDS is optimized either for light elements or heavy elements. In comparison with traditional WDS using the Rowland circle, parallel beam WDS systems can collect more X-ray counts under the same SEM conditions, but exhibit lower energy resolution than traditional WDS.

3.3 Electron Backscatter Diffraction and Applications

Electron backscattered diffraction (EBSD) is a technique which allows crystallographic information to be obtained from samples in SEM. In EBSD a stationary electron beam strikes a tilted crystalline sample and the diffracted electrons form a pattern on a fluorescent screen. This pattern is characteristic of the crystal structure and orientation of the sample region from which it was generated. The diffraction pattern can be used to measure the crystal orientation, measure grain boundary misorientation, discriminate crystal structures between different materials, and provide information about local crystalline imperfections. When the electron beam is scanned in a grid across a polycrystalline sample, the resulting map will reveal the constituent

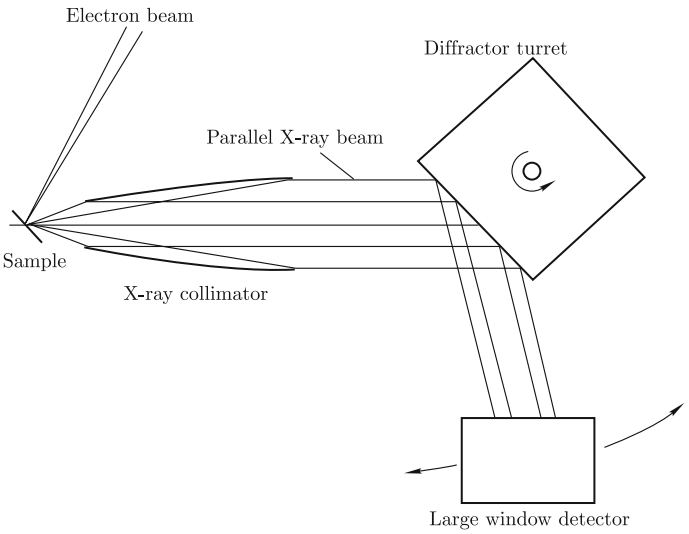

Fig. 20 Diagram of parallel beam WDS optics (Parallax Research Inc. 2013)

grain morphology, orientations, and boundaries. This data can also be used to show the preferred crystal orientations (texture) present in the material. A complete and quantitative representation of the sample microstructure can be established with EBSD.

1. History in brief

EBSD like patterns were first observed by Nishikawa and Kikuchi in TEM in 1928 Schwartz et al. (2009). Kikuchi found that electron diffraction patterns from thin films of mica contained the expected diffraction spots on a background of linear structures, which consisted of pairs of parallel excess and defect lines, now known as Kikuchi lines. Venables and Harland Schwartz et al. (2009) observed EBSD in SEM by using a 30 mm diameter fluorescent imaging screen and a closed circuit television camera which gave an angular range of $\sim 60°$. This method allowed on-line examination of specimens and the measurement of crystal orientation at high spatial resolution. Later, Dingley developed the combination of phosphor and television camera, and combined them with a graphical overlay. This allowed an operator to indicate the positions of zones in an EBSD and the software to display a simulation. Using this method, several hundreds of grain orientations could be measured in a day.

Software improvements lead to more intelligent analysis packages, e.g. CHANNEL that could analyze an EBSD from knowledge of the possible phases present. Application of the Hough transform allowed EBSD orientation measurements to be automated. Through the 1990s, automation of EBSD systems became increasingly common. Although initially slow, by 1996 automated systems could index at rates

of 4–5 patterns per second, although this was generally applied to higher symmetry phases. EBSD systems could by this stage take control of the SEM beam and, sometimes, the stage as well. This allowed the routine mapping of large areas on the surface of samples, but this often took many hours.

By the end of the 1990s the reliability of indexing and camera sensitivity had improved enough to make orientation mapping of more complex materials, such as geological samples, a reality. However, the speed of such systems was still limited by hardware and rarely exceeded 10 patterns per second.

The development of faster frame grabbers, computers and then the launch of fully digital CCD cameras in early 21st century has had a dramatic effect on the speed of the EBSD technique. At the end of first decade the maximum speed of data acquisition leapt from 100 patterns per second to more than 600 patterns per second. At the time of writing this chapter, it is reported that the acquisition speed reaches 1000 patterns per second. Orientation maps could now be acquired in a short time, typically 10–30 min for a statistically representative dataset. The reason for this dramatic speed increase is mostly due to the improved performance of the new digital detectors-these have an order of magnitude more sensitivity and also the capability of pixel binning for increased speed.

2. EBSD basics

The principal components of an EBSD system are shown in Fig. 21.

In a SEM chamber, a sample is tilted 70° from the horizontal towards a phosphor screen. The phosphor screen is fluoresced by electrons from the sample to form the diffraction pattern. A sensitive charge coupled device (CCD) video camera is placed behind the phosphor screen to view the diffraction pattern on it. A vacuum interface is needed for mounting the phosphor screen and camera in an SEM port. The camera monitors the phosphor through a lead glass screen in the interface, and the phosphor can be retracted to the edge of the SEM chamber when not in use. Electronic hardware is required to control the SEM, including the beam position, stage, focus, and magnification. A computer is used to control EBSD experiments, analyze the diffraction pattern and process and display the results. An optional electron detector mounted below the phosphor screen for electrons scattered in the forward direction from the sample can also be used.

For EBSD, a beam of electrons directly bombard a point of interest on a tilted crystalline sample in the SEM (Fig. 22). The mechanism by which the diffraction patterns are formed is complex, but the following model describes the principal features. The atoms in the material inelastically scatter a fraction of the electrons, with a small loss of energy, to form a divergent source of electrons close to the surface of the sample. These electrons are diffracted to form a set of paired large angle cones corresponding to each diffracting plane. When used to form an image on the fluorescent screen, the regions of enhanced electron intensity between the cones produce the characteristic Kikuchi bands of the electron back scattered diffraction pattern.

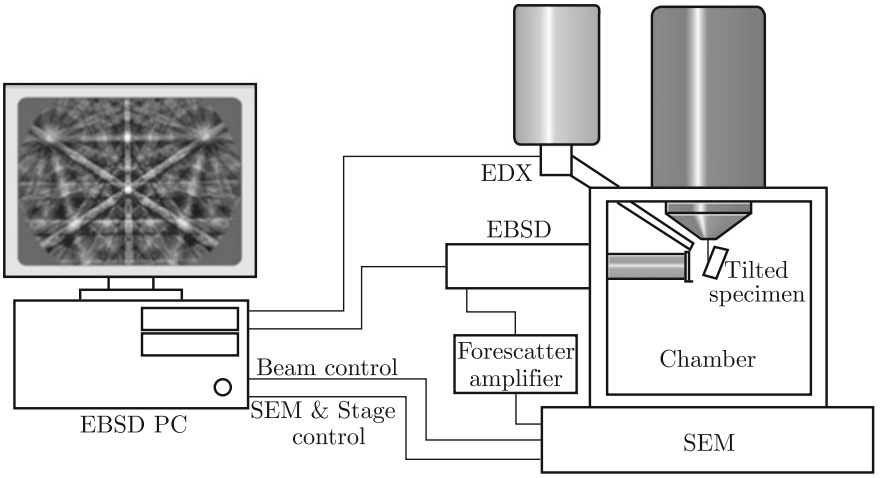

Fig. 21 Diagram showing the components of an EBSD system on SEM

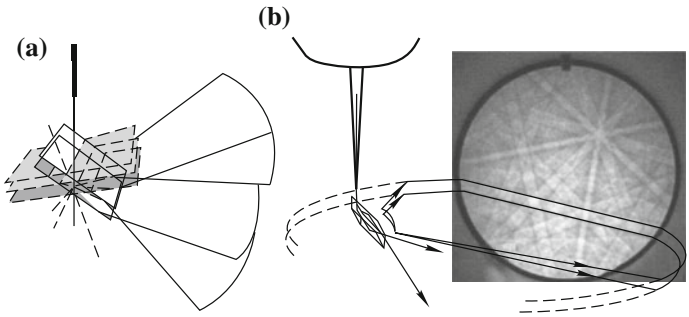

Fig. 22 The interaction of an electron beam with a crystal (**a**) and the formation of an EBSD pattern on phosphor screen (**b**)

The mechanisms giving rise to the Kikuchi band intensities and profile shapes are complex. As an approximation, the intensity of a Kikuchi band I_{hkl} for the (hkl) plane is given by

$$I_{\mathrm{hkl}} = \left[\sum_i f_i(\theta)\cos 2\pi(hx_i + ky_i + lz_i)\right]^2 + \left[\sum_i f_i(\theta)\sin 2\pi(hx_i + ky_i + lz_i)\right]^2 \quad (6)$$

where $f_i(\theta)$ is the atomic scattering factor for electrons and x_i, y_i, z_i are the fractional coordinates in the unit cell for atom i. An observed diffraction pattern should be compared with a simulation calculated using Eq. (6), to ensure only planes that produce visible Kikuchi bands are used when solving the diffraction pattern. This is especially important when working with materials with more than one atom type.

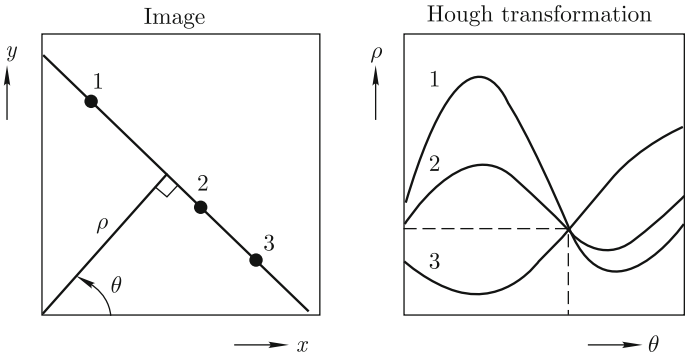

Fig. 23 The Hough transformation coverts lines into points in Hough space. The set of all straight lines going through a point in the (x, y) plane corresponds to a sinusoidal curve in the (ρ, θ) plane, Thus, a straight line formed by a set of points could be characterized by the intersection point of related sinusoids

In indexing EBSD patterns, the Kikuchi band must firstly be positioned. The central lines of the Kikuchi bands correspond to the intersection of the diffracting planes with the phosphor screen. Hence, each Kikuchi band can be indexed by the Miller indices of the diffracting crystal plane which formed it. The intersections of the Kikuchi bands correspond to zone axes in the crystal and can be labeled by zone axis symbols. The crystal orientation is calculated from the Kikuchi band positions by the computer processing the digitized diffraction pattern collected by the CCD camera. The Kikuchi band positions are found using the Hough transform (Hough 1962). The transform between the coordinates (x, y) of the diffraction pattern and the coordinates (ρ, θ) of Hough space is given by Eq. (7):

$$\rho = x \cos\theta + y \sin\theta \tag{7}$$

A straight line is characterized by ρ, the perpendicular distance from the origin and θ, the angle made with the x-axis and, so is represented by a single point (ρ, θ) in Hough space. The transformation is shown in Fig. 23.

Hough transformation makes Kikuchi band detection fast and reliable. Kikuchi bands transform to bright regions in Hough space which can be detected and used to calculate the original positions of the bands. The angles between the planes producing the detected Kikuchi bands can be calculated. These are compared with a list of inter-planar angles for the analyzed crystal structure to allocate Miller indices to each plane. The final step is to calculate the orientation of the crystal lattice with respect to coordinates fixed in the sample. This whole process takes less than a few milliseconds with modern computers.

3. Applications on materials research

In EBSD point analysis the beam is positioned at a point of interest on the sample, a diffraction pattern is collected and then the crystal orientation is calculated. In crystal orientation mapping, the electron beam is scanned over the sample on a grid of points and at each point a diffraction pattern is obtained and the crystal orientation is measured. The resulting data can be displayed as a crystal orientation map and processed to provide a wide variety of information about the sample microstructure.

The diffuseness or quality of the diffraction pattern is influenced by a number of factors including local crystalline perfection, surface contamination and the phase and orientation being analyzed. Pattern quality maps will often reveal features invisible in the electron image such as grains, grain boundaries and surface damage. The typical applications of EBSD in materials research are summarized in the following paragraphs.

Phase discrimination: EBSD can be used to distinguish crystallographically different phases and to show their location, abundance and preferred orientation relationships. EBSD can discriminate crystallographically dissimilar phases by comparing the interplanar angles measured from the diffraction pattern, with calculated angles from a set of candidate phases, and selecting the best fit. For phase identification, EDS will be firstly used to investigate the chemical information, then a rapid search for possible phases in databases based on the constituent elements is performed. Finally,

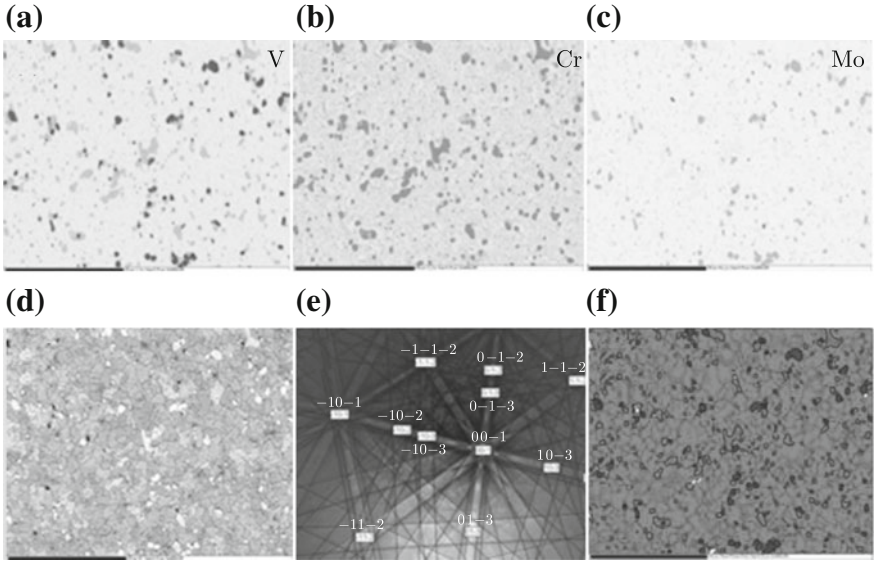

Fig. 24 Phase discrimination by EBSD. **a–d** Elemental mapping as recorded with EDS. **e** EBSD pattern of $C_{45}Mo_{18}V_{37}$ phase. **f** EBSD map revealing the phase distribution of ferrite (red), $C_{45}Mo_{18}V_{37}$ (blue) and Cr_7C_3 (green)

EBSD patterns are used to search the best fit from candidate phases. For phases with the same crystal structure, EDS will be used to help phase discrimination. Figure 24 shows the inclusions in a tool steel. To investigate the carbide types in this tool steel, EBSD mapping is performed with 4 phases selected-ferrite (Fe-BCC), austenite (Fe-FCC), M_7C_3 and $M_{23}C_6$ structures. Simultaneously EDS counts for 3 elements (Cr, Mo, V) are taken. After EBSD mapping, two phases were identified in this sample: austenite matrix with $M_7C_3(Cr_7C_3)$ inclusions. However, from the element maps of Mo, Cr, and V, it was realized that the Mo and V rich areas were something else other than austenite. By investigating the composition of the Mo and V rich area using EDS, these areas were re-indexed as $C_{45}Mo_{18}V_{37}$ with the same FCC structure as austenite. Finally, the phases in this sample were all identified correctly as shown in Fig. 24f.

Grain size and grain boundary analysis: Unlike an optical or scanning electron micrograph, the crystal orientation map must reveal the positions of all grains and grain boundaries in the sample microstructure. In crystal orientation maps a grain is defined by the collection of neighboring pixels in the map, which have a misorientation less than a certain threshold angle. The distribution of grain sizes can be measured from the data collected for the map. In addition, the distribution of grain boundary misorientation angles can also be shown. Figure 25 shows the orientation map, grain boundary angle distribution and grain size measured from a Nickel alloy.

Grain boundaries are characterized by the misorientation axis and angle and the boundary plane. Some boundaries satisfy certain geometrical criteria and their presence in a material may confer particular properties. When crystal lattices share a fraction of sites on either side of a grain boundary, they are termed coincident site lattices (CSL). CSLs are characterized by Σ, where Σ is the ratio of the size of the CSL unit cell to the standard unit cell. An example of special boundaries is shown in Fig. 26. In this figure grain boundary positions are superimposed on the pattern quality image (a). The boundaries are color coded according to the histogram of misorientation angle (b).

Texture and deformation analysis: Grains are seldom oriented randomly in polycrystalline materials. The preferred crystallographic orientation or texture of polycrystalline materials influences many properties of the bulk material, because physical properties are often anisotropic with respect to crystal direction. Material processing methods are frequently deliberately chosen to produce certain desired textures.

The individual crystal orientation measurements collected by crystal orientation mapping can be used to show the crystallographic textures developed in the sample. Figure 27 shows a texture map of a deformed Cu sample, in which various textures in the sample can be separated automatically, their volume fractions could be calculated, and the regions of the sample from which they originate is shown. Texture is usually measured by X-ray diffraction. EBSD is an ideal technique for microtexture analysis. In characterizing texture, compared with XRD, EBSD provides not only the types and percentages of textures, but also the microstructure information, such as distribution and grain size for certain texture. However, advances in EBSD pro-

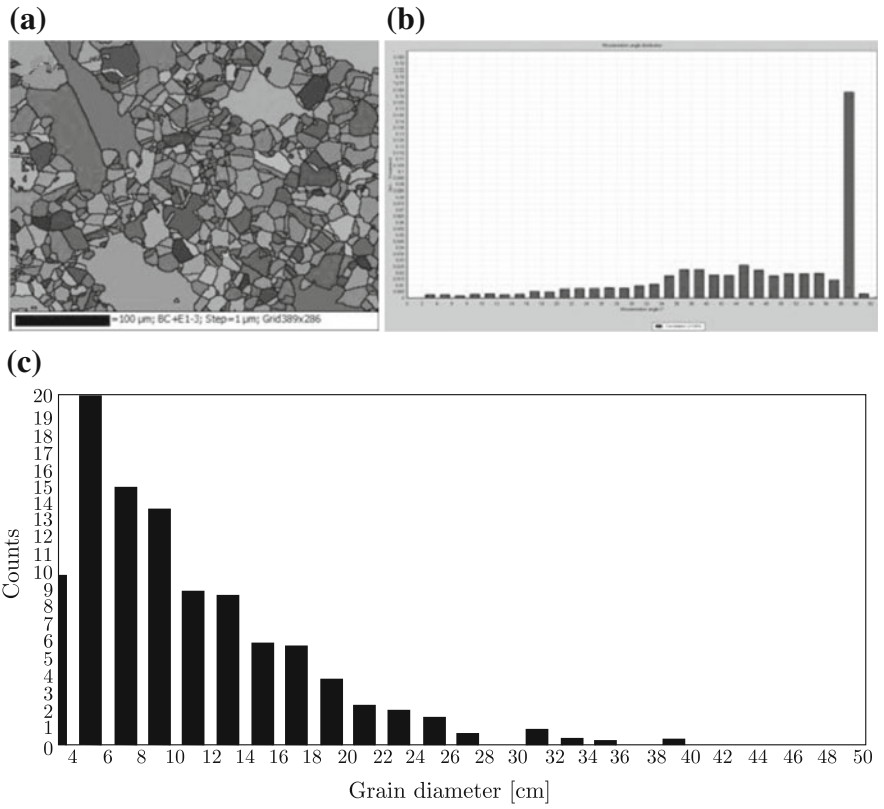

Fig. 25 **a** The orientation map showing grains with different orientation in different color, **b** grain boundary angle distribution and **c** grain size distribution in a Nickel alloy

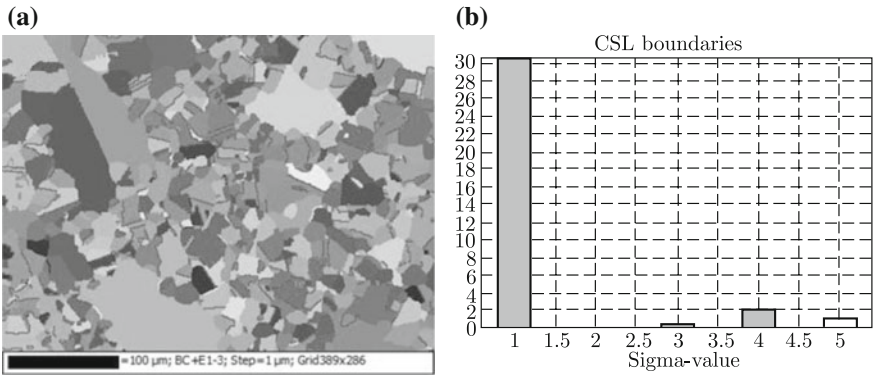

Fig. 26 **a** Coincident site lattice (CSL) boundary positions superimposed on the pattern quality image. **b** The boundaries are color coded by CSL type shown in the histogram of CSL

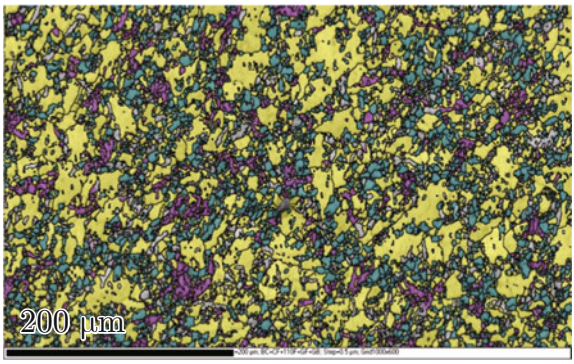

Fig. 27 Texture map of a deformed Cu sheet: 52% cubic fiber (yellow), 24% gamma fiber (teal) and 9% ⟨110⟩ fiber (purple) with 20° deviation, image courtesy of Oxford Instruments application notes

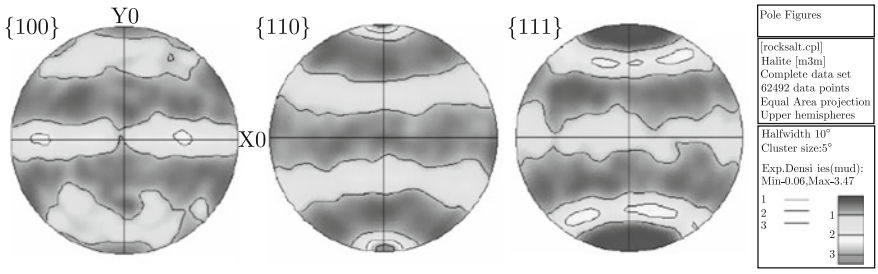

Fig. 28 Pole figures calculated from EBSD data from a nickel sample

cessing speed can make the technique competitive with X-ray diffraction for texture measurements for large samples. EBSD and X-ray diffraction are complementary techniques for texture analysis.

Traditionally, texture is usually measured by X-ray diffraction and illustrated by pole figure. The X-ray intensity from a particular diffracting plane is measured, while the sample is stepped through a series of orientations to complete the pole figure. The individual crystal orientations measured with EBSD can also be displayed as pole figures for preferred orientation analysis, as shown in Fig. 28.

EBSD mapping can also be used to illustrate the deformation within a grain. As shown in Fig. 29a, the inverse pole figure (IPF) color coded orientation map shows the lattice rotation within a grain. Since the orientation at each pixel is measured by EBSD in an orientation map, a local misorientation map (misorientation with respect to neighboring pixels) can be used to visualize subtle low angle grain boundaries, which is beyond the capability of pure grain boundary mapping, after removing orientation noise by certain filters. Figure 29b illustrates these low angle sub-grain boundaries within a grain.

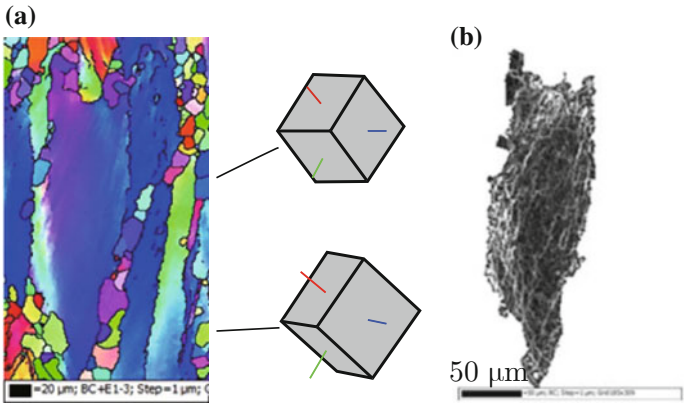

Fig. 29 **a** IPF orientation map of deformed nickel, and **b** local misorientation map showing the sub-grain low angle boundaries

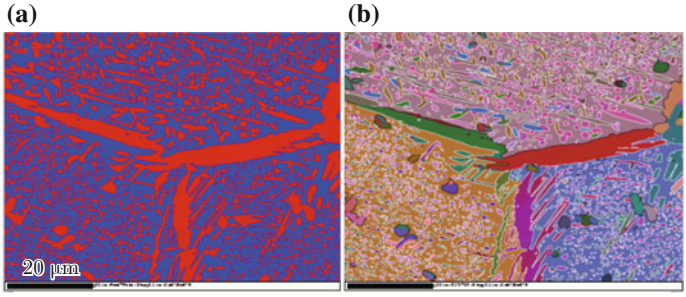

Fig. 30 **a** Phase map and **b** orientation map of the sample

Orientation relationship verification by EBSD: After the orientations of different phases is measured by EBSD, the orientation relationship between these phases can be determined or verified. The interface between FCC and BCC crystals can be found in many important metallic alloys. The orientation relationships (OR) between these two phases often show a deviation from the exact Kurdjumov-Sachs relationship (K-S OR), Nishiyama-Wassermann relationship and so on; the close packed planes in the FCC and BCC phases are usually parallel to or nearly parallel to each other. To verify the OR between two phases, interphase boundaries can be plotted overlayed onto the image, as shown in Fig. 30. In Fig. 30b the K-S OR interface boundaries are plotted in white. If the deviation from K-S OR is over 7° the interface boundaries are in black. From the map we can see that most of particles show a K-S OR matrix.

4. Spatial resolution and measurement accuracy

The electrons contributing to the diffraction pattern originate within nanometres of the sample surface. Hence, the spatial resolution will be related to the electron beam diameter, and this depends on the type of electron source and probe current used. Typical beam diameters at 0.1 nA probe current and 20 kV accelerating voltage are 2 nm for a FEG source, and 30 nm for a tungsten source. The beam profile on the sample surface will also be elongated in the direction perpendicular to the tilt. The spatial resolution achieved in practice will depend on the sample, SEM operating conditions and electron source used, and under optimum conditions, grains as small as 10 nm can be identified.

Errors in crystal orientation measurements from the diffraction pattern will depend principally on the accuracy of the Kikuchi band position measurement and the system calibration, and are generally in the range ±0.3°. Recently, with the advance of the EBSD pattern indexing algorithm, a method called refined accuracy indexing brings the orientation measurement error down to below ±0.1°, which will be very useful to reveal the subgrain structures in materials. An example in Fig. 31 shows data from a single grain in an Al alloy. This material has been deformed 20% and annealed at 200 °C for 0.5 h. EBSD data has been collected from a part of this grain and indexed using refined accuracy. Local average misorientation maps are used to show the detailed microstructure. With refined accuracy the images are less noisy and more detail is visible.

5. Sample preparation for EBSD

For EBSD analysis, the sample surface should be prepared very carefully since it is very sensitive to crystalline perfection, and some treatments may be needed to remove any surface damage. A well prepared sample is a prerequisite for obtaining

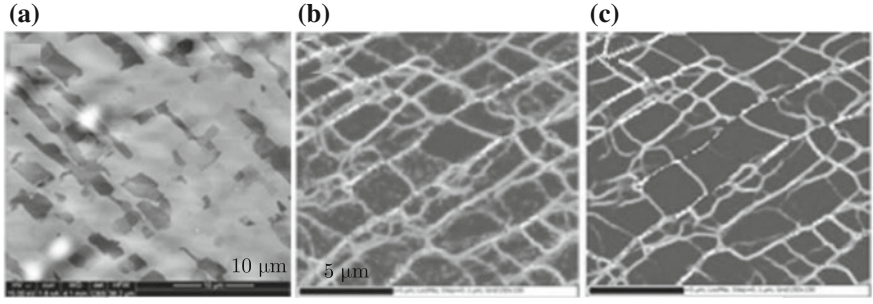

Fig. 31 **a** The BSE image shows that the single crystal has developed deformation bands with very low angle boundaries; **b** Local misorientation map processed using conventional EBSD indexing method, and **c** Local misorientation map processed using refined accuracy showing the clear subgrain structures. Image courtesy of Oxford Instruments application notes

a good diffraction pattern. Surfaces must be sufficiently smooth to avoid forming shadows on the diffraction pattern from other parts of the sample.

Different materials may require suitable techniques to prepare. For metals and insulators the typical procedure should be mounting in conductive resin, mechanical grinding, diamond polishing and final polishing with colloidal silica. For metals electropolishing is also a useful method for final polishing. Brittle materials such as ceramics and geological materials can often be fractured to reveal surfaces immediately suitable for EBSD. Ion milling can be used for materials which are not amenable to conventional metallography such as zirconium and zircalloy. Dual focused ion beam–electron beam microscopes fitted with EBSD can perform in situ specimen preparation for EBSD. Plasma etching can be used for microelectronic devices.

Charging in non-conductive samples can be eliminated, as for X-ray microanalysis, by the deposition of a conducting layer. The deposited layer must be very thin, for example 2–3 nm of carbon, otherwise a diffraction pattern will not be obtained. It may be necessary to increase the electron accelerating voltage to penetrate the conducting layer. Charging can be reduced when the sample is tilted for EBSD experiments and can also be reduced by analyzing the sample in an environmental or low vacuum SEM.

References

Ardenne, M.V.: Das elektronen-rastermikroskop (in German). Zeitschrift für Phys. **109**(9–10), 553–572 (1938)

Andrasko, J., Maehly, A.C.: Detection of gunshot residues on hands by scanning electron microscopy. J. Forensic Sci. 279–287 (1977)

Amelinckx, S., van Dyck, D., van Landuyt, J., van Tendeloo, G.: Handbook of Microscopy, pp. 539–561. VCH Verlagsges (1997)

ASTM Standard guide for gunshot residue analysis by scanning electron microscopy/energy dispersive X-ray Spectrometry, Designation: E1588–07 (2007)

Everhart, T.E., Thornley, R.F.M.: Wide-band detector for micro-micro-ampere low-energy electron currents. Adv. Imag. Elect. Phys. **133**, 147–152 (1960)

FEI announces new verios extreme high resolution SEM (2012). Nanotechnology Now

Goldstein, J., Newbury, D. E., Echlin, P., Joy, D. C., Romig, Jr. A. D., Lyman, C. E., Fiori, C., Lifshin, E.: Scanning Electron Microscopy and X-Ray Microanalysis, 2nd edn. Plenum Press (1992a)

Goldstein, J., Newbury, D.E., Echlin, P., Joy, D.C., Romig Jr., A.D., Lyman, C.E., Fiori, C., Lifshin, E.: Scanning Electron Microscopy and X-ray Microanalysis, Chapter 2. Springer, New York (1992b)

Hitachi Launches World's Highest Resolution FE-SEM (2011). Nanotechnology Now

Hough, P.V.C.: Methods and means for recognizing complex patterns. US patent 3069654 (1962)

Joy, D.C.: Monte Carlo Modeling For Electron Microscopy and Microanalysis. Oxford University Press (1995)

Ketek, GmbH. http://dwww.ketek.net/products/sdd-technology/working-principle/ (2013)

Knott, G., Marchman, H., Wall, D., Lich, B.: Serial section scanning electron microscopy of adult brain tissue using focused ion beam milling. J. Neurosci. **28**(12), 2959–2964 (2008)

Li, H., Li, Y.M., Lei, Z.C., Wang, K.Y., Guo, A.K.: Transformation of odor selectivity from projection neurons to single mushroom body neurons mapped with dual-color calcium imaging. P. Natl. Acad. Sci. USA **110**(29), 12084–12089 (2013)
Oxford Instruments Silicon Drift Detectors Explained (2012)
Oxford Instruments Technique brief, Energy dispersive X-ray microanalysis hardware (2002)
Oxford Instruments Technique brief, Wavelength dispersive X-ray microanalysis (2004)
Parallax Research Inc. http://www.parallaxray.com/wds.html (2013)
Schwartz, A.J., Kumar, M., Adams, B.L., Field, D.P.: Electron Backscatter Diffraction in Materials Science, 2nd edn. Springer, New York (2009)
Smith, K.C.A., Johari, O. (eds.) Proceedings of the 5th Annual SEM Symposium, IITRI, Chicago (1972)
Zhou, W.L., Wang, Z.L.: Scanning Microscopy for Nanotechnology. Springer, New York (2007)